

Observation of planar oscillations of MeV protons in silicon using ion channeling patterns

M. B. H. Breese, P. J. C. King, and G. W. Grime

SPM Unit, Nuclear Physics Laboratory, Keble Road, University of Oxford, Oxford, OX1 3RH, United Kingdom

P. J. M. Smulders

Nuclear Solid State Physics, Materials Science Centre, Groningen University, Nijenborgh 4, 9747 AG Groningen, The Netherlands

L. E. Seiberling and M. A. Boshart

Department of Physics, 215 Williamson Hall, University of Florida, Gainesville, Florida 32611-2085

(Received 17 August 1995; revised manuscript received 6 November 1995)

This paper describes the observation of $\{110\}$ planar oscillations of 3 MeV protons transmitted through a 0.5 μm thick $[001]$ silicon crystal using ion channeling patterns produced on a fluorescent viewing screen. Gradual variations in the crystal thickness allowed the exit angular distribution of the protons to be sampled at different depths into the crystal, revealing effects due to the coherent planar oscillations. This work necessitated the use of a focused MeV proton beam from a nuclear microprobe to generate channeling patterns from selected, micron-size regions and the necessary ion optics are developed here. The recorded channeling patterns are interpreted with the help of Monte Carlo computer simulations.

I. INTRODUCTION

MeV ions which are incident along a major crystal axis or plane have a channeled trajectory, in which they oscillate back and forth in regions of lower electron density between the channel walls. This results in a lower rate of energy loss and a lower nuclear encounter probability than for ions which have a nonchanneled trajectory.¹⁻³ The maximum angle of an ion's path to the channel walls for which channeling will take place when the ion is incident in the center of a channel is called the channeling critical angle ψ_c .^{1,2,4} The measurement of the backscattered ion, x-ray, or nuclear reaction yields in channeled and nonchanneled alignment gives information on the crystalline quality, layer epitaxy, impurity atom lattice location, amount of lattice strain, etc. Comprehensive accounts of many aspects of the theory and applications of MeV ion channeling using unfocused beams are given in Refs. 1 and 2.

There are many ion channeling phenomena which rely on an understanding of planar oscillation amplitudes, wavelengths, and depth of coherency for a proper interpretation, such as impurity lattice site location¹ and various forms of strain measurements.⁵ The recent development of spatially resolved channeling images of dislocations and stacking faults⁶⁻¹⁰ using a nuclear microprobe has further increased the need for a better understanding of planar oscillation phenomena. This is because it is essential for an accurate interpretation of the observed channeling image contrast as a function of tilt angle, particularly with the present development of nuclear microprobes capable of spot sizes less than 100 nm. There has, however, been no previous studies on the visual observation of planar oscillations through thin crystals as a function of tilt angle away from channeling alignment.

This paper describes the production and interpretation of high angular resolution "selected area" and "convergent beam" channeling patterns to observe coherent oscillations of 3 MeV protons through the $\{110\}$ planes of a 0.5 μm thick

silicon crystal, which had a gradual thickness variation across it. This work is motivated by the wish to characterize planar oscillations using ion channeling patterns, to develop the understanding of how a focused, convergent ion beam can influence channeling alignment, and to produce and explain previously unobserved effects of planar oscillations in channeling patterns.

Section II develops the ion optical basis necessary to produce and interpret selected area and convergent beam channeling patterns generated using a nuclear microprobe, and how the channeling alignment can be altered by varying the tilt angle of the incident beam. The effects of planar oscillations observed in channeling patterns recorded at different beam convergence and tilt angles to the $\{110\}$ planes of a thin silicon crystal are described in Sec. III. Section IV gives Monte Carlo computer simulations which verify the observed behavior.

A. Previous work using ion channeling patterns

One of the first confirmations of the effect of crystal structure on ion trajectories through matter was the production of "blocking" or "star" patterns using collimated, unfocused MeV ion beams. The angular intensity distribution of ions scattered in forward or backward directions out of a crystal can be observed on a fluorescent viewing screen,^{11,12} captured using photographic film or cellulose nitrate foils,¹³ or recorded using position-sensitive or scanned particle detectors.^{14,15}

If the recording medium is placed at a backward scattering angle for the beam, blocking patterns are produced.¹⁶ Blocking¹⁷ refers to the process by which ions emitted from lattice sites (such as those scattered through large angles owing to close nuclear collisions) have a decreased probability of being emitted along channeling directions. The ion paths are steered away from the channeling directions by the same correlated series of small-angle scatterings which produces

channeling. The angular locations of crystal planes and axes thus appear as regions of reduced intensity in the angular distribution.

For patterns recorded in transmission using thin crystals, an increased intensity of transmitted ions is produced where the incident beam is aligned with a channeling direction.¹⁸ Channels away from the beam direction again show a reduced intensity owing to blocking.

There has been considerable development of the use of channeling patterns to identify different types of crystal structures, as described in Ref. 16 and Chap. 11 of Ref. 1. Other work on measuring and interpreting channeling patterns includes Gemmell and Holland^{17,19} who investigated blocking effects and measured the relationship between the observed planar channel linewidth and the incident beam energy. Dearnaley *et al.*¹⁸ used channeling patterns to characterize the potential barrier which exists between axial and planar channeling. Feldman and Appleton³ studied multiple scattering and planar dechanneling of MeV protons transmitted through thin silicon and germanium wafers. Armstrong and co-workers^{20,21} used a “supercollimated” MeV proton beam of spot size 25 μm to study the transverse motion of axially channeled ions. This facilitated the generation of channeling patterns where the angle subtended by the beam spot on the viewing screen was small enough not to limit any observed structure, which had been a feature of many previously published patterns.

Rosner²² used a two-dimensional position-sensitive charged-particle detector to generate images showing the intensity distribution of MeV protons transmitted through silicon crystals less than 1 μm thick. The “doughnut” distribution of transmitted ions produced when the beam was tilted slightly away from a major axis was measured and interpreted in terms of variations in the transverse proton momentum. Krause and Nesković used two-dimensional position sensitive detectors to observe the “rainbow” effect produced by the passage of $\langle 110 \rangle$ and $\langle 100 \rangle$ axially channeled MeV ions through crystals less than 0.2 μm thick.^{23,24}

This paper presents a comprehensive set of channeling patterns produced from a 0.5 μm thick [001] silicon crystal from selected areas of less than 1 μm across, using a focused proton beam with differing incident beam convergence and tilt angles, so that proton oscillations as a function of beam-crystal alignment angle can be observed.

B. Previous work on planar oscillations

Planar channeled MeV ions undergo an oscillatory motion in which they move back and forth in regions of lower electron density between the channel walls. The oscillation wavelength for each ion, λ , is dependent on the ion’s initial impact parameter with the channel walls when it enters the crystal; those ions with the smallest resultant oscillation amplitudes have the longest wavelengths. However, the variation in wavelengths is small enough for coherency between the individual channeled ion paths to be maintained for some depth into the crystal, typically several oscillation wavelengths. Ions incident with the beam aligned with a planar channel are initially focused into the center of the channel by their collisions with the first few atom layers. They cross the channel center at a depth of $\lambda/4$ along their trajectory, travel to the opposite channel wall and are then focused back into

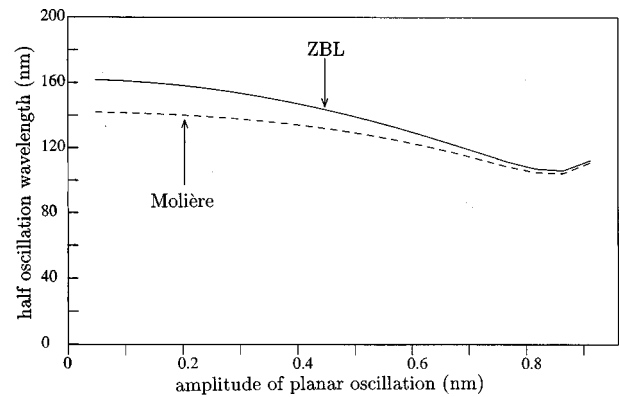


FIG. 1. Half-wavelength for 3 MeV protons oscillating in the $\{110\}$ planes of silicon, as a function of amplitude of the motion.

the channel center at a depth of $3\lambda/4$. This behavior continues, but owing to the spread in wavelengths and the effects of multiple scattering as the ions pass through the crystal, the coherency breaks down with increasing depth. Statistical equilibrium is reached when the flux distribution becomes independent of depth (assuming no dechanneling).

Figure 1 shows the half-wavelength for 3 MeV protons oscillating in the $\{110\}$ planes of silicon, as a function of the amplitude of the motion. These results were obtained by a numerical integration of the equations of motion that follow from the ZBL (Ziegler-Biersack-Littmark) and the Molière potentials. In both cases, thermally modified planar continuum potentials were used^{14,25} in which the atomic planes are approximated by a uniform density distribution, convoluted in the direction perpendicular to the plane with a Gaussian distribution to account for thermal vibrations. In both potential models, the results were summed over a number of adjacent planes. From Fig. 1, the ZBL and Molière potentials give respectively a wavelength for very low amplitude oscillations of approximately 320 and 280 nm.

Axial channeling is not considered in this paper because the more complicated oscillations of the ions are in two dimensions, and the effects of coherency are lost rapidly with depth into the crystal.^{23,24}

Experimentally, the effects of planar oscillations have been observed in the transmitted energy spectra of ions passing through thin crystals when a highly collimated detector was used to select ions with certain oscillation wavelengths, as described in Chap. 6 of Ref. 1. Small variations in crystal thickness and mosaic spread were recognized as limiting the ability to measure oscillations in such work using an unfocused ion beam.^{26,27} Oscillations can also be observed in backscattering spectra of MeV He ions, as the variation in flux distribution across a channel with depth leads to a changing probability of close nuclear collisions.²⁸ This has not been observed for backscattering MeV protons owing to insufficient detector energy resolution. Plots of the nuclear encounter probability (see Sec. IV) as a function of depth produced using computer simulations of planar channeling also enable the effects of oscillations to be observed.²⁵ The transition from coherent oscillations to statistical equilibrium has been studied,²⁹ and coherent oscillations have been used to characterize the strain in superlattice structures using a process called “catastrophic dechanneling.”³⁰

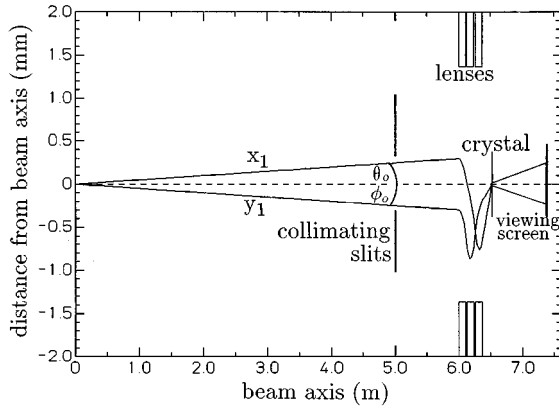


FIG. 2. Schematic of the focusing action of the Oxford nuclear microprobe, which uses a triplet of quadrupole lenses. The 3 MeV proton beam diverges from the object aperture at the origin on the beam axis. The divergence into the quadrupole lenses is collimated by the slits located 5 m from the object. The proton trajectory (x_1, y_1) with $\theta_0=0.003^\circ$ the horizontal (x) direction, and $\phi_0=-0.003^\circ$ in the vertical (y) direction is shown. The location of the viewing screen used to observe the channeling patterns is indicated but its size is not to scale.

There have been no previous systematic observations of planar oscillations using channeling patterns. This is because of the stringent conditions this necessitates, which are a crystal approximately $0.5 \mu\text{m}$ thick, the ability to position a very small beam spot at well located areas and the need to alter the proton path length by at least $\lambda/4$, corresponding to a thickness change of about 75 nm for 3 MeV protons in the $\{110\}$ planes of silicon. A method whereby planar oscillations might be observed in channeling patterns is to tilt a uniformly-thin crystal within a plane so that the path length of the channeled protons is increased. This, however, imposes very stringent conditions for maintaining the same channeling alignment over the required tilt range, which may be tens of degrees. A different method is used in this paper whereby a focused MeV proton beam is stopped at different points across a $0.5 \mu\text{m}$ thick silicon crystal which has a thickness variation of approximately $\pm(\lambda/2)$ across its surface, owing to the preparation method.

II. ION OPTICAL CONSIDERATIONS

The effects of the focusing action of a nuclear microprobe on channeling alignment is considered in this section in order to combine ion channeling and ion optics into a cohesive framework.

A nuclear microprobe uses 2–4 magnetic quadrupole lenses to focus a low-divergence MeV light ion beam passing through an object aperture into a small spot with a higher convergence angle on the crystal surface, as shown in Fig. 2. The beam divergence half-angle from the object aperture is θ_0 in the horizontal (x) direction and ϕ_0 in the vertical (y) direction; on the Oxford microprobe, they can be separately adjusted using four independent slit jaws mounted on micrometers. The ion optics of nuclear microprobes are fully described in Refs. 31 and 32. It suffices to say here that the focusing action of the quadrupole multiplet results in the beam on the crystal surface being a demagnified image of the

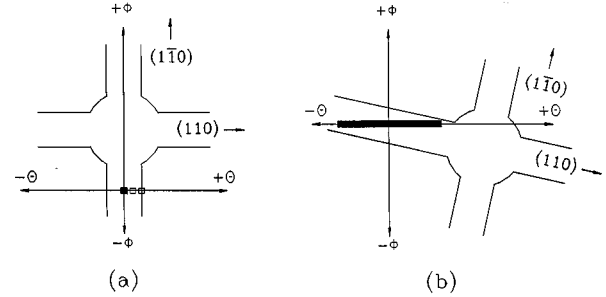


FIG. 3. Angular representations of the beam convergence and tilt angle on the surface of a $[001]$ crystal, for which only the $\{110\}$ planes are shown. The ion beam axis through the lenses is located at $\theta=\phi=0$ mrad. The angular extent of the beam convergence in the horizontal beam direction is $+\theta_i$ to $-\theta_i$; similarly in the vertical direction the extent is $+\phi_i$ to $-\phi_i$. (a) Beam channeled in the $(\bar{1}10)$ planes but not the (110) planes. A low beam convergence in the horizontal and vertical directions, and centered on the beam axis is shown by the solid square. Other examples of similar ranges of beam convergence which make beam tilt angles of $\theta_i=+0.06^\circ$ and $+0.12^\circ$ to the $(\bar{1}10)$ planes are shown as the hollow squares to the right of the solid square. In (b) the crystal has been rotated clockwise by 8° about the axis, and tilted so that the beam axis is aligned with the (110) planes. The beam has a convergence angular range of $\theta_i=\pm 0.5^\circ$ and $\phi_i=\pm 0.02^\circ$, as shown by the solid rectangle.

object aperture, with a convergence half-angle of $\theta_i=D_x\theta_0$ in the x direction and $\phi_i=D_y\phi_0$ in the y direction, where D_x, D_y are the demagnifications in the x and y directions, respectively. The Oxford nuclear microprobe, shown in Fig. 2, uses a triplet configuration of quadrupole lenses³³ with demagnifications of $D_x\sim 80$ and $D_y\sim 23$, so for the same beam divergence angles θ_0, ϕ_0 , the beam convergence angles in the vertical and horizontal directions on the crystal surface are different. The channeling patterns shown in Figs. 5 and 6 in Sec. III have been generated using typical values of $\theta_0, \phi_0\sim 5\times 10^{-4}$ to 3×10^{-3} deg, giving beam convergence half-angles which can be varied between $\theta_i, \phi_i\sim 0.01^\circ$ to 0.10° . The channeling patterns in Fig. 7 were generated using a considerably larger convergence half-angle of $\theta_i=0.5^\circ$, as described below. The focused beam spot size on the crystal surface was less than $1 \mu\text{m}$ and contained a proton beam current of approximately 100 pA.

The crystal studied in this work was mounted on a goniometer which allows translation and rotation about horizontal and vertical axes in the sample plane.⁷ This enables planar and axial channeling directions to be located with an accuracy of $\pm 0.03^\circ$. Figure 3(a) shows angular representations of the focused proton beam convergence and tilt angle on the $[001]$ crystal surface. The location of the crystal planes and axes on this angular coordinate system depends on the orientation of the $[001]$ axis with respect to the beam axis. In Fig. 3(a) the crystal (110) planes are parallel to the horizontal direction and the crystal $(\bar{1}10)$ planes are parallel to the vertical direction. The crystal $[001]$ axis is rotated in the vertical direction away from alignment with the beam axis, which is thus aligned with the $(\bar{1}10)$ but not the (110) planes. The spacings between the lines of the crystal planes and axes in Fig. 3 correspond to twice the planar or axial channeling angles. For 3 MeV protons channeled in the silicon $\{110\}$ planes, the measured half width at half maximum of the

transmitted energy curve as a function of tilt angle is $\psi_{1/2}=0.10^\circ$, whereas the channeling critical angles are $\psi_c=0.15^\circ$ using the Molière interatomic potential, and $\psi_c=0.14^\circ$ using the ZBL potential.

Different ion optical conditions associated with the effect of the incident beam convergence and tilt angle on the interpretation of the resultant channeling pattern are now described. The beam convergence shown in Fig. 3(a) by the solid box is centered on the beam axis, and is small compared with the planar channeling critical angle. The resultant channeling pattern is produced from a selected, micron-sized area of the crystal. Since a focused proton beam is used the angular resolution of the channeling pattern is not degraded by the lateral extent of the beam spot at the viewing screen.

Virtually all previous ion channeling analyses have involved tilting the crystal sample with respect to an incident unfocused MeV ion beam in order to measure crystalline properties.^{1,2} However, in work on crystal defect imaging using spatially resolved ion channeling in conjunction with a nuclear microprobe,⁶⁻¹⁰ a major problem has been that the feature of interest gradually shifted across the analyzed area with increasing crystal tilt angle, owing to the lack of perfect eucentricity of the goniometer. An important aspect of the measured channeling patterns showing planar oscillations in the $\{110\}$ planes described in Sec. III, is the approach used to overcome this problem. Here the tilt angle of the incident focused beam is altered with respect to a fixed crystal orientation. Consider the hollow squares shown in Fig. 3(a) to the right of the solid square. These show different beam tilt angles with respect to the beam axis and consequently also give different beam tilt angles with respect to the $(1\bar{1}0)$ crystal planes. This approach is achieved in practice by shifting the location of the horizontal collimator slits, shown in Fig. 2. The resultant channeling patterns produced with these different beam tilt angles are all from the same micron-size region of the crystal surface.

In Fig. 3(b) the crystal has been tilted and rotated about the $[001]$ axis so that the (110) and $(1\bar{1}0)$ planes are not aligned with the horizontal and vertical beam directions. The beam convergence angular range shown by the solid rectangle has $\theta_i > \psi_c$ but $\phi_i \ll \psi_c$, so all the incident beam is aligned within a tilt angle of less than ψ_c to the (110) planes and all hits the same micron-size region on the crystal surface. The incident beam makes different tilt angles to the (110) planes with changing horizontal convergence angle, which influences the contrast observed within the resultant channeling pattern. Such a “convergent beam” channeling pattern may thus be defined as one in which the observed intensity distribution is affected by a large incident beam convergence, in one or both directions. Such channeling patterns are shown below in Fig. 7, where they allow the effect of a gradually changing beam tilt angle to the crystal $\{110\}$ planes to be observed.

III. EXPERIMENTAL RESULTS

A. Experimental procedure

The crystal which was used to observe coherent planar oscillations was a thin, self-supporting $[001]$ silicon crystal, prepared at the University of Florida according to the method developed by Cheung.³⁴ Boron was diffused into one side of

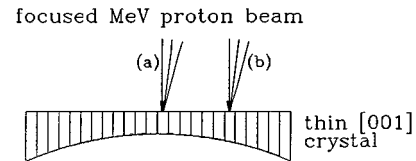


FIG. 4. Schematic of a focused proton beam incident at two points on the surface of the thin crystal where the thickness gradually changes with lateral position (this is idealized and greatly exaggerated). The incident beam tilt angle can be altered with respect to the crystal orientation, such as the three tilt angles shown at points (a) and (b). The crystal is shifted laterally to observe channeling patterns at a slightly different crystal thickness.

a blank silicon wafer at about 1000°C to act as an etch stop, then a masked area was selectively etched to produce a dislocation-free thin layer. There was no detectable variation of the crystallographic orientation across the crystal using this procedure.

A feature of this preparation method is that the crystal thickness varies slightly. For the best prepared crystals the measured thickness typically varies by $\pm 5\%$. On other similarly prepared crystals the thickness variation can be much larger. For the crystal used here, an average thickness of $0.5 \pm 0.1 \mu\text{m}$ was determined by measuring the transmitted energy loss of $7.5 \text{ MeV } ^{16}\text{O}$ ions. The thickness variation of about $\pm 100 \text{ nm}$ thus corresponds approximately to $\pm (\lambda/2)$ for 3 MeV protons in the $\{110\}$ planes of silicon, allowing one complete period of oscillation to be studied. Figure 4 shows a schematic of the focused MeV proton beam incident at two points on the surface of this crystal. In order to generate channeling patterns from different thicknesses, the crystal was shifted laterally, such as from points (a) to (b) in Fig. 4.

In Sec. III B, the absolute crystal thickness at which each channeling pattern was recorded was not known since it was not possible to measure nanometer thicknesses using 3 MeV protons, owing to insufficient detector energy resolution. Therefore the approach used in comparing the observed channeling patterns with Monte Carlo computer simulations in Sec. IV is to compare the measured and simulated results over a complete period of the observed behavior.

The channeling patterns were produced on a fluorescent viewing screen consisting of willemite ($\text{ZnSiO}_4:\text{Mn}$), located 680 mm downstream of the crystal, as shown in Fig. 2. The patterns were each photographed using 25 ASA technical pan black and white film with a 30 second exposure. Two $+4$ diopter lenses were used to enlarge the patterns on the camera film.

B. Measured ion channeling patterns

Figure 5 shows channeling patterns recorded from eight sequential, micron-size regions across this crystal surface, labeled (a) to (h). First, consider the set of channeling patterns measured at $\theta_i=0.0^\circ$, which correspond to the beam-crystal alignment shown in Fig. 3(a) by the solid square. The location on the crystal from which each sequential channeling pattern was produced was chosen arbitrarily to give a different transmitted angular distribution; these same loca-

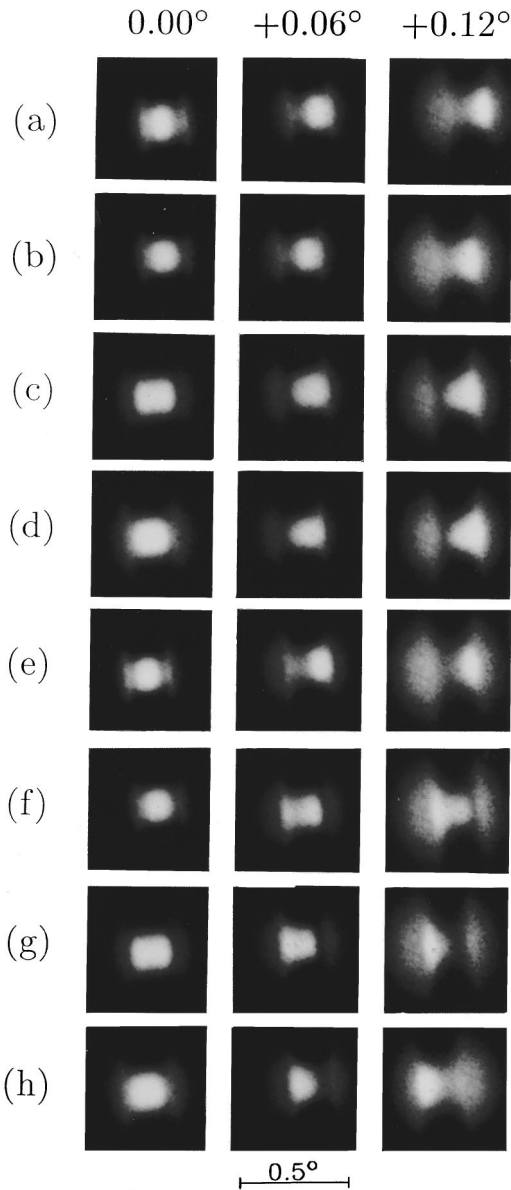


FIG. 5. Channeling patterns measured from eight sequential, micron-size regions across the $0.5 \mu\text{m}$ thick silicon crystal surface, labeled (a) to (h). The three beam tilt angles used are $\theta_i = 0.0^\circ, +0.06^\circ, +0.12^\circ$ to the $(1\bar{1}0)$ planes. The beam convergence angles are $\pm 0.02^\circ$ in both directions.

tions were then used for the patterns measured at other beam tilt angles. At the first crystal thickness, (a), most of the beam transmitted through the crystal has a very low emergent angle, with two side-lobes containing smaller fractions of beam with a larger emergent angle. At a different crystal thickness, (b), the observed central bright spot enlarges until it merges with the two sidelobes to form a continuous bright band, (c). With a further change in crystal thickness, (d), the bright band decreases in size, and becomes similar to the first pattern in (e) and (f). With further changes in crystal thickness, a similar sequence of increasing size of the bright spot is repeated in patterns (g) and (h) until the bright spot again becomes a minimum, similar to that shown in pattern (a), and is not shown here.

The observed contrast in these channeling patterns is due to the oscillations of the proton beam. These oscillations are

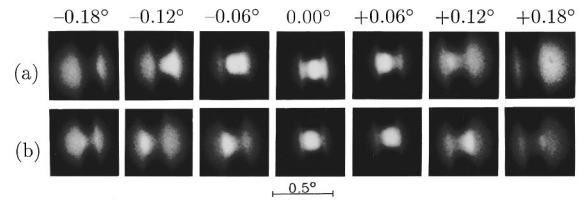


FIG. 6. Channeling patterns as a function of tilt angle of the incident beam through alignment with the $(1\bar{1}0)$ planes from two slightly different crystal thicknesses, (a) and (b). The beam convergence angles are $\pm 0.02^\circ$ in both directions.

initially coherent, so that there are depths when the majority of the protons are at the centers of the $(1\bar{1}0)$ channels, and intermediate depths when they are at the walls of the $(1\bar{1}0)$ channels. When the protons are bunched at the channel center, they have a maximum emergent angle, such as pattern (c), and when they are close to the channel walls they have a minimum emergent angle, such as pattern (a).

The sets of channeling patterns in Fig. 5 which were measured at the beam tilt angles of $\theta_i = +0.06^\circ, +0.12^\circ$ correspond to the alignments shown by the hollow squares in Fig. 3(a). In these patterns in Figs. 5(a) and 5(b) the transmitted beam has a positive emergent angle (i.e., to right of the channel center); for $\theta_i = +0.12^\circ$, the beam has a larger positive angle than for $\theta_i = +0.06^\circ$. In (c) and (d) the beam is starting to emerge with a smaller positive angle. In (e) the beam again has a positive emergent angle. However in (f) some beam emerges with a negative angle (i.e., to the left of the channel center). This also occurs in (g), (h) before the beam again moved back to the same positions shown in (a), again not shown.

In Fig. 5, two complete periods of similar oscillatory behavior are observed for $\theta_i = 0.0^\circ$; one period from patterns (a) to (e), and the other period from patterns (f) back through to (a). However, for the patterns recorded at $\theta_i = +0.06^\circ, +0.12^\circ$ there is only one period of behavior observed over the full thickness variation represented in these patterns.

Figure 5 shows the effects of planar oscillations at three different beam tilt angles with respect to the $(1\bar{1}0)$ planes for gradually changing crystal thicknesses. Figure 6 shows channeling patterns at two different crystal thicknesses for different beam tilt angles to the $(1\bar{1}0)$ planes. Both locations were chosen to give a small spot in the channel center at $\theta_i = 0.0^\circ$. In Fig. 6(a) the beam emerges with an angle to the right of center of the $(1\bar{1}0)$ planes for $\theta_i = -0.12^\circ$, and emerges with an angle increasingly towards the left of center with further positive tilt angle. In Fig. 6(b) the beam emerges with an angle to the left of center of the $(1\bar{1}0)$ planes at a beam tilt angle of $\theta_i = -0.12^\circ$, and emerges with an angle increasingly towards the right of center with further positive tilt angle.

Figure 7 shows convergent beam channeling patterns from sequential, micron-size areas across the $0.5 \mu\text{m}$ thick crystal surface, which demonstrate the effect of smaller incremental changes in the beam tilt angle to the channeling planes. For these patterns the horizontal collimator slits were opened to $\pm 550 \mu\text{m}$ to give a beam convergence angular range of $\theta_i = \pm 0.5^\circ$ on the crystal surface. The (110) planes were aligned with the beam axis and the crystal was rotated clockwise by 8° about its surface normal $[001]$ axis. The

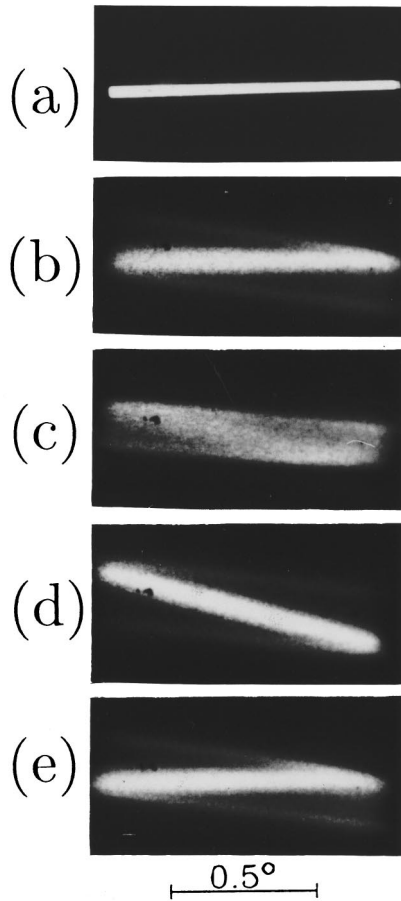


FIG. 7. Convergent beam channeling patterns from sequential, micron-sized areas of the crystal. The beam convergence angles are $\theta_i = \pm 0.5^\circ$, $\phi_i = \pm 0.02^\circ$. The (110) crystal planes are rotated clockwise by 8° from the beam horizontal and vertical directions, as in Fig. 3(b). (a) shows the measured extent of the beam convergence on the crystal surface. Two small marks can be seen on the viewing screen in the middle left region in (b) to (e), so the shift in the emergent angle of the transmitted beam can be judged from this reference.

horizontal beam convergence progressively made a different tilt angle of up to $\pm 0.07^\circ$ to the (110) planes, as shown in Fig. 3(b).

Figure 7(a) just shows the measured extent and orientation of the incident beam convergence on the crystal (which was removed for this photograph). In Fig. 7(b) the beam transmitted through the crystal emerges with the same angular distribution as it went in, i.e., the same alignment as in Fig. 7(a). In Fig. 7(d) the beam transmitted through the crystal has been rotated clockwise compared with Fig. 7(b); Fig. 7(c) shows an in-between situation occurring at an intermediate crystal thickness. In Fig. 7(e) the beam transmitted through the crystal emerges with the same angular distribution as in Fig. 7(b), representing one complete period of observed behavior. The origin of this behavior is described in Sec. IV, where the different oscillation wavelengths of channeled protons making different tilt angles to the channeling planes is considered.

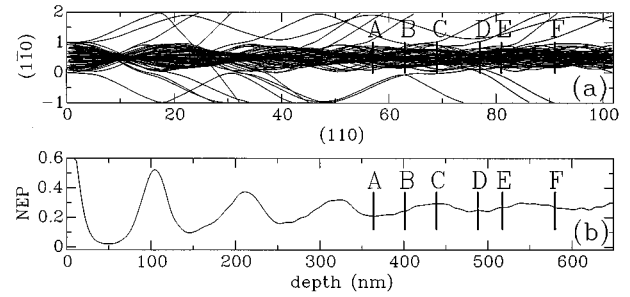


FIG. 8. (a) Simulated trajectories of a hundred 3 MeV protons, with the beam aligned with the (110) planes. The plot axes are labeled in units of the (110) and $(\bar{1}\bar{1}0)$ interplanar distances, and the plot projection is described in the text. The approximate lateral x distance reached by the protons transmitted through the crystal is $650 \text{ nm} \times \tan 1.73^\circ / 0.192 \text{ nm} = 102$ (110) plane units. On the vertical scale, all the protons enter the crystal between the bounding planes at locations 0.0 and 1.0. (b) NEP versus depth for 3 MeV protons (110) planar channeled. The plot is shown only for NEP values less than 0.6 so that the small oscillations for depths greater than 400 nm can be seen. Points A–F in these two plots correspond to the sample thicknesses used for the distributions shown in Fig. 9.

IV. COMPUTER SIMULATION OF ION CHANNELING PATTERNS

Computer simulation was used to verify the origin of the behavior of the channeling patterns in Sec. III. The Monte Carlo code FLUX3,^{35–37} which uses the ZBL potential, was used to simulate the angular distribution of protons transmitted through a thin silicon crystal. The incident proton beam was aligned with or close to the $(\bar{1}\bar{1}0)$ planes, and 1.73° away from the [001] crystal normal direction. In order to produce plots of the angular distribution of the transmitted protons, an angular region centered on the $(\bar{1}\bar{1}0)$ channeling planes, was subdivided into 100×100 bins. A bin was incremented for each transmitted proton according to the proton's exit velocity vector. The code also allowed the trajectories of individual protons to be followed through the crystal by periodic output of the proton's x and y coordinates. A coordinate system with the z axis along the crystal [001] direction, and the x and y axes along the crystal [100] and $[\bar{1}10]$ directions, respectively, was used. Trajectories were produced by plotting a proton's x coordinate versus its y coordinate; this was therefore effectively a plot of the projection of the protons' paths on to the (001) plane normal to the channeling planes. The tilt angle of 1.73° to the [001] axis meant that a proton at a depth d had an x coordinate given approximately by $d \times \tan 1.73^\circ$. A given x coordinate does not correspond to a specific depth into the crystal for each proton, however, owing to the fact that each proton does not remain at an angle of exactly 1.73° to the axes. The x and y coordinates were converted into $\{110\}$ planar distances by division by 0.192 nm; the x coordinate is therefore given in terms of (110) interplanar distances, and the y coordinate in terms of $(\bar{1}\bar{1}0)$ channeling plane distances.

Figure 8(a) shows the trajectories of 100 protons aligned with the (110) planes through the first 650 nm of a silicon crystal. Close to the crystal surface, the strong focusing effect of the channeling planes can be seen, with most of the

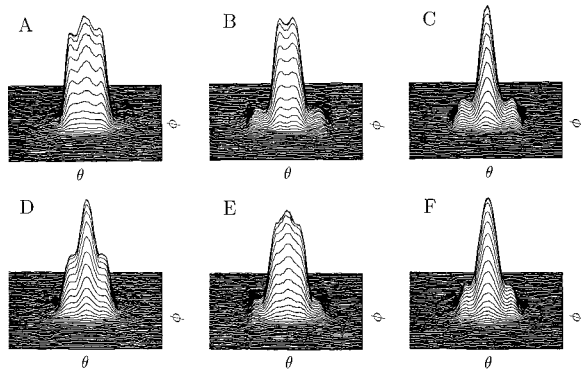


FIG. 9. Simulated three-dimensional angular distributions of 3 MeV protons transmitted through a thin silicon crystal for various crystal thicknesses corresponding to the points A–F in Fig. 8. Each plot encompasses an angular range of $0.5^\circ \times 0.5^\circ$. The (110) planes run parallel to the vertical (ϕ) beam direction. Each plot was produced using 50 000 protons and has been smoothed to show the distribution more clearly.

protons being steered into the channel center at an x coordinate of about 10 (equivalent to them having traveled one quarter of their oscillation wavelength). The protons are close to the channel walls at $x=20$ and are brought back to the channel center at $x=30$. For larger x values, the coherency between the proton trajectories begins to break down, primarily because of the variation in proton oscillation wavelengths, with those protons with lowest amplitude having the longest wavelengths. This loss of coherency is overemphasized in Fig. 8(a) as a given x coordinate does not correspond to a specific depth for each proton, as stated above.

Figure 8(b) shows the average nuclear encounter probability (NEP) of thirty thousand protons with the incident beam channeled in the $(1\bar{1}0)$ planes, again plotted over a sample thickness range of 650 nm. The NEP (Refs. 25 and 38) is the probability for nuclear encounters, as a function of depth, relative to the probability in a “random system,” as defined by Eqs. (8) and (9) of Ref. 38. The NEP plot will be dominated by the ions with the largest oscillation amplitudes, as these come closest to the channel walls. It starts at 1.0 at the crystal surface, and falls rapidly to a low value after a depth of 50 nm. This depth corresponds to the protons being focused into the channel center. The NEP oscillates with depth, with the minima occurring where the proton trajectories cross the channel center and the maxima being where the protons are close to the channel walls. The amplitude of the NEP oscillations dies away with depth, owing to the loss in coherency between the proton trajectories. Oscillations are still clearly visible to depths of over 600 nm, demonstrating that some coherency is retained throughout this thickness of crystal.

Figure 9 shows three-dimensional renditions of computer simulations of the angular distributions of 3 MeV protons transmitted through crystals of six different thicknesses, for $\theta_i=0.0^\circ$. Each thickness A–F is marked on the plots of Fig. 8. The thickness range encompassed in Fig. 9 corresponds approximately to that used to produce the measured channeling patterns shown in Figs. 5–7. In these plots, the $(1\bar{1}0)$ planar channel is running parallel to the vertical (ϕ) beam direction so that changing the horizontal (θ) beam direction

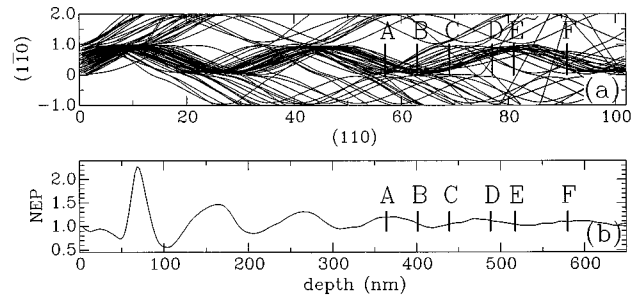


FIG. 10. (a) Simulated trajectories of a hundred 3 MeV protons incident at $\theta_i=+0.12^\circ$ to the $(1\bar{1}0)$ planes. (b) NEP plot for 3 MeV protons incident at $\theta_i=+0.12^\circ$ to the $(1\bar{1}0)$ planes.

would move the beam in angle through the $(1\bar{1}0)$ planes. Figure 9(a) shows the distribution corresponding to a minimum in the NEP plot. This occurs when the majority of channeled protons are crossing the channel center where they are at the steepest angle with respect to the channel walls. The distribution therefore fills quite uniformly the whole of the angular width of the channel, and has a full width at half maximum (FWHM) of 0.15° . This corresponds to the measured pattern shown in Fig. 5(c) where a broad, uniform distribution across the channel is also observed.

Figure 9(c) shows the distribution corresponding to a crystal thickness at the next maximum of the NEP plot. In this case, there is a peak observed in the distribution in the channel center with FWHM of 0.06° . At this thickness, most of the channeled protons are close to the bounding planes, so that their trajectories are making only small angles with the planes. It should be noticed, however, that some protons were transmitted within two sidelobes which peak at 0.08° from the channel center. The base of the distribution is wider than that shown in Fig. 9(a). This corresponds to the measured patterns shown in Figs. 5(a) and 5(e) where there are also two sidelobes about narrow distribution in the channel center. Figure 9(b) shows a distribution for a crystal with thickness intermediate between those of (a), (c), and corresponds to the measured channeling pattern shown in Fig. 5(b).

The plots of Figs. 9(d)–9(f) are from thicker regions of the crystal and were performed for thicknesses corresponding again to roughly minima, intermediate and maxima of the NEP plot. They show a similar set of three distributions as in Figs. 9(a)–9(c), demonstrating that coherent oscillations continue out to beyond crystal thicknesses of 580 nm. However, the correspondence between the NEP plot and the trajectory plot is less obvious owing to the decrease in coherency with increasing penetration depth. This is because the NEP is not a good indicator for determining the behavior of the remaining channeled, coherent beam fraction, since it is dominated by those ions with a large oscillation amplitude as described above. The change from a broad distribution to one that is highly peaked at the channel center occurs twice over the thickness range used in Fig. 9 for $\theta_i=0.0^\circ$, just as there are two complete periods of change observed in Fig. 5 at planar alignment.

Figure 10 shows proton trajectories and an NEP plot similar to those of Fig. 8, but for a beam tilt angle of $\theta_i=+0.12^\circ$ to the $(1\bar{1}0)$ channeling planes. The NEP rises to a value well above 1.0 at a depth of 70 nm, corresponding to the protons

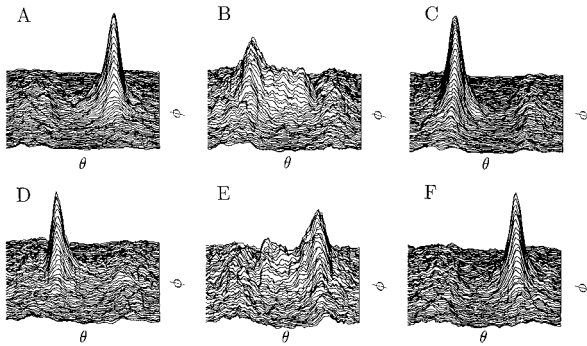


FIG. 11. Simulated three-dimensional angular distributions of 3 MeV protons transmitted through silicon crystals with thicknesses as given by points A–F in Fig. 10. Each plot encompasses an angular range $0.5^\circ \times 0.5^\circ$. The $(1\bar{1}0)$ planes run parallel to the vertical (ϕ) beam direction. The proton beam is incident at $\theta_i = +0.12^\circ$ to the $(1\bar{1}0)$ planes.

meeting the channel walls for the first time. At this point, many protons pass through the walls; most of these do not channel but some are still channeled and describe stable oscillations at a higher-positioned channel. A similar effect can be seen when the protons approach the bottom wall. Of those which are reflected from the channel wall, it can be seen that their trajectories remain coherent to depths beyond 600 nm again. The NEP plot at this tilt angle shows minima every time the protons cross the channel center. However, unlike the case for exact planar alignment of the incident beam, at these points most of the protons are all traveling in similar directions toward one side of the channel.

Simulated angular distribution plots for the same crystal thicknesses as used in Fig. 9 but with a beam tilt angle of $\theta_i = +0.12^\circ$ to the $(1\bar{1}0)$ planes, are given in Fig. 11. Figure 11(a) shows a peak in the distribution with the majority of the protons emerging at an angle of 0.13° to the right of center of the $(1\bar{1}0)$ planes. The corresponding position on the trajectory plot in Fig. 10(a) shows the majority of channeled protons travelling in the same direction towards the lower plane. As the crystal thickness is increased, the distribution changes to show the protons emerging to the left of center of the $(1\bar{1}0)$ planes in Fig. 11(c). The transition of the protons from emerging on one side of channeling alignment to emerging on the other occurs at a maximum in the NEP plot for this beam angle, shown in Fig. 11(b). At this point, the protons are closest to the channel walls, and begin their journeys back to the other side of the channel. Figures 11(d)–11(f) show the transition of the beam back to emerging to the right of center of the $(1\bar{1}0)$ planes, for crystal thicknesses out to 580 nm. At this beam tilt angle, the change in the distribution from emerging on one side of the channeling direction to the other side occurs only once, as also observed in Fig. 5.

Consider further the agreement between the simulated patterns in Figs. 9 and 11, and the measured patterns in Fig. 5. At a crystal thickness where there is a very narrow emergent angular range for $\theta_i = 0.0^\circ$ in Fig. 9(c), for a beam tilt angle of $\theta_i = +0.12^\circ$ the beam emerges to the left of center within the $(1\bar{1}0)$ planes in Fig. 11(c) in the simulated pattern. Similar behavior is observed in the measured patterns in Fig. 5(f). At a slightly greater crystal thickness the angular distri-

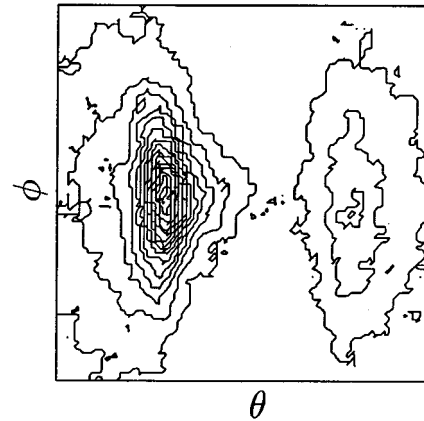


FIG. 12. Contour plot of the simulated distribution shown in Fig. 11(c). The box size is $0.5^\circ \times 0.5^\circ$ and the proton beam is incident at $\theta_i = +0.12^\circ$ to the $(1\bar{1}0)$ planes.

bution within the $(1\bar{1}0)$ planes becomes much broader in Fig. 9(d) for $\theta_i = 0.0^\circ$, while for $\theta_i = +0.12^\circ$ the beam still emerges to the left of center within the $(1\bar{1}0)$ planes in Fig. 11(d). This is also observed in Fig. 5(g). With further increase in crystal thickness the simulated pattern for $\theta_i = 0.0^\circ$ exhibits a maximum distribution across the channel in Fig. 9(e), while for $\theta_i = +0.12^\circ$ the beam begins to emerge to the right of center within the $(1\bar{1}0)$ planes in Fig. 11(e), as is also seen in Fig. 5(h). Finally, in Fig. 9(f) there is again a narrow angular distribution for $\theta_i = 0.0^\circ$ and in Fig. 11(f) the beam has flipped emerging to the right of center within the $(1\bar{1}0)$ planes for $\theta_i = 0.12^\circ$, as can be seen in Fig. 5(a).

Now consider the agreement between the simulated patterns in Figs. 9 and 11 and the measured patterns in Fig. 6. At crystal thicknesses where there is a very narrow emergent angular range for $\theta_i = 0.0^\circ$ in Figs. 9(c) and 9(f), the beam emerges to the left of center within the $(1\bar{1}0)$ planes in Fig. 11(c) and to the right of center in Fig. 11(f) for $\theta_i = +0.12^\circ$ in the simulated plots. Similar behavior is also observed in the measured patterns in Fig. 6.

The three-dimensional plots in Figs. 9 and 11 have been shown to exhibit similar behavior as the measured channeling patterns in Figs. 5 and 6. Further agreement can be shown by displaying the simulated data in Fig. 11(c) as a contour plot in Fig. 12. This can be compared with the channeling patterns shown in Fig. 5(f) or 5(g) for $\theta_i = +0.12^\circ$. In both cases, the intensity distribution is peaked at an angle of 0.10° to the left of center of the $(1\bar{1}0)$ planes, and forms an “arrowhead” shape, pointing into the channel center. The simplest explanation for this arrowhead intensity distribution is that those protons remaining in the channel center spend the most time in regions of low atomic electron density. These well-channeled protons consequently make fewest collisions with the atomic electrons (and also with the nuclei comprising the channel walls), so undergo the least scattering, thus acquiring the least transverse momentum parallel to the channeling planes. Conversely, those protons which travel close to the channel walls acquire the highest transverse momentum and so have the widest intensity distribution parallel to the channeling planes. This results in those well-channeled protons emerging with a low transverse exit

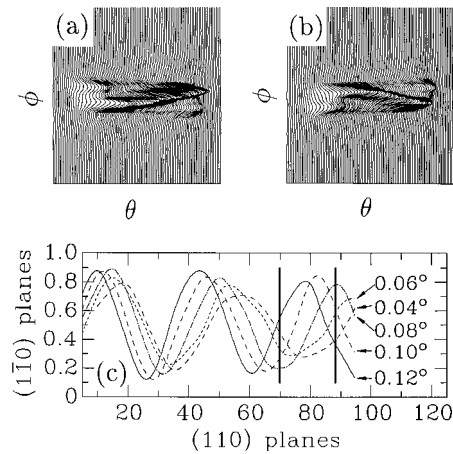


FIG. 13. (a), (b) Simulated three-dimensional angular distributions over an angular range of $1.5^\circ \times 1.5^\circ$ for two crystal thicknesses corresponding to points (c) and (d) in Fig. 10. The proton beam has a uniform convergence angular range between $\theta_i = \pm 0.5^\circ$ (with $\phi_i = 0.0^\circ$) and the crystal has been rotated about its normal direction by 11.0° , similar to the orientation shown in Fig. 3(b). (c) shows average trajectories of channeled protons with a coherent path through 600 nm of a silicon crystal for beam angles between 0.04° and 0.12° to alignment. The two heavy vertical lines mark the crystal thicknesses used for the two simulated angular distributions in (a), (b).

angle, and those less well channeled protons emerging with a higher transverse exit angle, giving the observed distribution.

The simulated angular distributions in Fig. 13 investigate the origin of the behavior observed in the convergent beam channeling patterns in Fig. 7. Figures 13(a) and 13(b) show the effect of a large horizontal beam convergence into the (110) planes, which are slightly misaligned with the horizontal beam direction, similar to the conditions used to produce the measured convergent beam patterns shown in Fig. 7. Plots are shown for two crystal thicknesses of 444 nm in Fig. 13(b), and 562 nm in Fig. 13(a).

As with the measured patterns, the angular distribution of the protons is flipped in the simulated patterns from one side of the channel center to the other as the crystal thickness changes. This is due to the different depth at which the coherent proton oscillations were sampled, as described above. In Fig. 13(a), for small beam tilt angles to the channeling planes there is a fairly linear relationship between exit and incident angles. This occurs for beam angles to alignment of up to 0.06° , where the pattern becomes slightly “S” shaped, whilst some of the beam begins to appear on the other side of the channeling direction. A similar situation occurs in Fig. 13(b), with the switch to the other side of the channeling direction occurring at a tilt angle of about 0.08° . No evidence is seen of this in Fig. 7, because the beam tilt angle to the channeling planes is not larger than 0.07° .

In order to better understand these plots, simulations of proton trajectories similar to those shown in Figs. 8 and 10 were performed for beam tilt angles to the (110) planes up to 0.12° , in 0.02° steps. In the trajectory plot of Fig. 10(a), which was performed for an incident beam angle of $\theta_i = 0.12^\circ$, there is a set of channeled trajectories which remain reasonably coherent over the depth range of the plot. It has been assumed that this strongly coherent group is prima-

riarily responsible for oscillation effects seen in the measured and simulated channeling patterns. It is thus possible to draw on Fig. 10(a) a line which represents the “average” trajectory of this coherent group, so that the average distribution as a function of depth could be determined. This average trajectory has been plotted in Fig. 13(c) for beam tilt angles of 0.04° to 0.12° . Trajectory plots for tilt angles less than 0.04° [such as Fig. 8(a)] tended not to show a single, average trajectory and so were not included in Fig. 13(c). As may be expected, the wavelength of the average trajectory plots decreases as the beam tilt angle to the channeling direction increases in Fig. 13(c).

Marked on the plot of Fig. 13(c) are two solid, dark lines at depths corresponding to the two crystal thicknesses used to produce the angular distribution plots of Figs. 13(a) and 13(b). Consider the thickness given by the line at a depth of seventy (110) plane distances, which corresponds to Fig. 13(b). The trajectories for beam tilt angles of 0.04° and 0.06° are heading towards the lower channel wall at this depth. For a tilt angle of 0.08° , the average trajectory is at a turning point close to where the protons meet the channel walls. For beam tilt angles of 0.10° and 0.12° , the average trajectory is moving towards the upper channel wall. It can therefore be seen that protons incident at angles of 0.06° or less to channeling alignment would be transmitted on one side of the channeling direction and that a transition would occur at a tilt angle of about 0.08° to protons being emitted on the other side of the channeling direction. This is what is seen to be the case in Fig. 13(b). The solid line at a depth of 88 (110) plane distances corresponds to Fig. 13(a). The average trajectories at this depth show a similar pattern to those at the first solid line. However, the directions of the average trajectory plots have changed on going from the first thickness to the second; the angular distributions therefore show a flip from one side of channeling alignment to the other, as observed in Fig. 7.

This rather crude method of displaying the coherent proton oscillations for different beam tilt angles adequately explains the observed convergent beam channeling patterns. It is, however, not intended to accurately convey differences in the proton oscillation amplitude since this was difficult to accurately determine from the trajectory plots.

V. CONCLUSIONS

We have described the observation of {110} planar oscillations of 3 MeV protons transmitted through a thin silicon crystal, using selected area and convergent beam channeling patterns. The origin of these patterns has been characterized using Monte Carlo computer simulations.

The use of a focused MeV proton beam from a nuclear microprobe to generate channeling patterns from selected areas with different beam convergence and tilt angles has been described and the ion optics needed to understand the focusing effects of a nuclear microprobe on the resultant pattern have been outlined. It should be noted, however, that our usage of the term “convergent beam” pattern is different to that underlying the production of convergent beam electron diffraction patterns, whereby the crystal is placed in between the image and focal planes.

This work is important since it gives the capability to observe and characterize other phenomena in a similar manner, such as ion channeling and dechanneling through strained layers and the generation of selected area channeling patterns from crystal defects.

ACKNOWLEDGMENTS

P. K. wishes to thank the Royal Commission for the Exhibition of 1851 for support. We also wish to acknowledge the excellent technical assistance of M. Marsh in Oxford.

- ¹ *Channeling, Theory, Observation and Applications*, edited by D. V. Morgan (Wiley, London, 1973).
- ² L. C. Feldman, J. W. Mayer, and S. T. Picraux, *Materials Analysis By Ion Channeling* (Academic, New York, 1982).
- ³ L. C. Feldman and B. R. Appleton, *Phys. Rev. B* **8**, 935 (1973).
- ⁴ J. K. Lindhard, *Dan. Vidensk. Selsk. Mat.-Fys. Medd.* **34** (14) (1965).
- ⁵ S. T. Picraux, B. L. Doyle, and J. Y. Tsao, *Semiconductors and Metals Vol. 33* (AT&T Bell Labs., New Jersey, 1991), Chap. 3.
- ⁶ M. B. H. Breese, P. J. C. King, J. Whitehurst, G. R. Booker, G. W. Grime, F. Watt, L. T. Romano, and E. H. C. Parker, *J. Appl. Phys.* **73**, 2640 (1993).
- ⁷ P. J. C. King, M. B. H. Breese, G. R. Booker, J. Whitehurst, P. R. Wilshaw, G. W. Grime, F. Watt, and M. J. Goringe, *Nucl. Instrum. Methods B* **77**, 320 (1993).
- ⁸ M. B. H. Breese, P. J. C. King, P. J. M. Smulders, and G. W. Grime, *Phys. Rev. B* **51**, 2742 (1995).
- ⁹ P. J. C. King, M. B. H. Breese, P. R. Wilshaw, and G. W. Grime, *Phys. Rev. B* **51**, 2732 (1995).
- ¹⁰ P. J. C. King, M. B. H. Breese, P. R. Wilshaw, and G. W. Grime, *Phys. Rev. Lett.* **74**, 411 (1995).
- ¹¹ G. O. Engelmohr, R. M. Mueller, and W. White, *Nucl. Instrum. Methods* **83**, 160 (1970).
- ¹² R. S. Nelson, *Philos. Mag.* **15**, 845 (1967).
- ¹³ D. A. Marsden, N. G. E. Johansson, and G. R. Bellavance, *Nucl. Instrum. Methods* **70**, 291 (1969).
- ¹⁴ R. B. Appleton, C. Erginsoy, and W. M. Gibson, *Phys. Rev.* **161**, 330 (1967).
- ¹⁵ W. M. Gibson, C. Erginsoy, H. E. Wegner, and B. R. Appleton, *Phys. Rev. Lett.* **15**, 357 (1965).
- ¹⁶ C. S. Barrett, R. M. Mueller, and W. White, *J. Appl. Phys.* **39**, 4695 (1968).
- ¹⁷ D. S. Gemmell and R. E. Holland, *Phys. Rev. Lett.* **14**, 945 (1965).
- ¹⁸ G. Dearnaley, I. V. Mitchell, R. S. Nelson, B. W. Farmery, and M. W. Thompson, *Philos. Mag.* **18**, 985 (1968).
- ¹⁹ D. S. Gemmell and R. E. Holland, *Phys. Rev.* **173**, 344 (1968).
- ²⁰ D. D. Armstrong, W. M. Gibson, and H. E. Wegner, *Radiat. Eff.* **11**, 241 (1971).
- ²¹ D. D. Armstrong, W. M. Gibson, A. Goland, J. A. Golovchenko, R. A. Levesque, R. L. Meek, and H. E. Wegner, *Radiat. Eff.* **12**, 143 (1972).
- ²² J. S. Rosner, W. M. Gibson, J. A. Golovchenko, A. N. Goland, and H. E. Wegner, *Phys. Rev. B* **18**, 1066 (1978).
- ²³ N. Nesković, *Phys. Rev. B* **33**, 6030 (1986).
- ²⁴ H. F. Krause, S. Datz, P. F. Dittner, J. Gomez del Campo, P. D. Miller, C. D. Moak, N. Nesković, and P. L. Pepmiller, *Phys. Rev. B* **33**, 6036 (1986).
- ²⁵ J. F. Barrett, *Phys. Rev. B* **3**, 1527 (1971).
- ²⁶ S. Datz, C. D. Moak, T. S. Noggle, B. R. Appleton, and H. O. Lutz, *Phys. Rev.* **179**, 315 (1969).
- ²⁷ F. H. Eisen and M. T. Robinson, *Phys. Rev. B* **4**, 1457 (1971).
- ²⁸ F. Abel, G. Amsel, M. Bruneaux, C. Cohen, and A. L'Hoir, *Phys. Rev. B* **12**, 4617 (1975).
- ²⁹ B. A. Davidson, L. C. Feldman, J. Bevk, and J. P. Mannaerts, *Appl. Phys. Lett.* **50**, 135 (1987).
- ³⁰ S. T. Picraux, W. R. Allen, R. M. Biefeld, J. A. Ellison, and W. K. Chu, *Phys. Rev. Lett.* **54**, 2355 (1985).
- ³¹ G. W. Grime and F. Watt, *Beam Optics of Quadrupole Probing Systems* (Hilger, Bristol, 1984).
- ³² M. B. H. Breese, D. N. Jamieson, and P. J. C. King, *Materials Analysis Using a Nuclear Microprobe* (Wiley, New York, 1996).
- ³³ G. W. Grime, M. Dawson, M. Marsh, I. C. McArthur, and F. Watt, *Nucl. Instrum. Methods B* **54**, 52 (1991).
- ³⁴ N. W. Cheung, *Rev. Sci. Instrum.* **51**, 1212 (1980).
- ³⁵ P. J. M. Smulders and D. O. Boerma, *Nucl. Instrum. Methods B* **29**, 471 (1987).
- ³⁶ P. J. M. Smulders, D. O. Boerma, and M. Shaanan, *Nucl. Instrum. Methods B* **45**, 450 (1990).
- ³⁷ A. Dygo, W. N. Lennard, I. V. Mitchell, and P. J. M. Smulders, *Nucl. Instrum. Methods B* **90**, 161 (1994).
- ³⁸ P. J. M. Smulders, *Nucl. Instrum. Methods B* **94**, 595 (1994).